Word count: 8737

Single-Crystal X-ray Diffraction on the Structure of (Al,Fe)-bearing

Bridgmanite in the Lower Mantle

- 4 Suyu Fu^{1,2,*}, Stella Chariton³, Yanyao Zhang¹, Takuo Okuchi⁴, Vitali B. Prakapenka³, Jung-Fu Lin^{1,*}
- ¹Department of Geological Sciences, Jackson School of Geosciences, The University of Texas at Austin,
- 6 Austin, TX, USA

2

3

- ²School of Earth and Space Exploration, Arizona State University, Tempe, Arizona, USA.
- 8 ³Center for Advanced Radiation Sources, The University of Chicago, Chicago, IL, USA
- ⁴Institute for Integrated Radiation and Nuclear Science, Kyoto University, Kyoto, Japan.
- *Corresponding author: Suyu Fu (<u>fsyxhy@gmail.com</u>), Jung-Fu Lin (<u>afu@jsg.utexas.edu</u>)

Abstract

11

12

13

14

15

16

17

18

19

20

21

22

23

24

The lattice parameters of (Al,Fe)-bearing bridgmanite, the most abundant lower-mantle mineral, are fundamental to our understanding of its thermoelastic and transport properties at high pressure and temperature (P-T). However, due to the complexity of Fe and Al substitution as well as the spin and valence states of Fe in the structure of bridgmanite, experimental refinements on its atomic positions are rather limited to relatively low pressure and/or to compositions not as relevant to the lower mantle. Here, we have performed single-crystal X-ray diffraction (SCXRD) experiments on two high-quality crystal platelets of (Al,Fe)-bearing bridgmanite (Mg0.88Fe³⁺0.065Fe²⁺0.035Al0.03)(Al0.11Si0.90)O3 (Fe10-Al14-Bgm), up to 64.6 GPa at room temperature in a Boehler-Almax type diamond anvil cell (DAC). Refinements on the collected SCXRD patterns reveal reliable structural information of single-crystal Fe10-Al14-Bgm, including unit-cell parameters, atomic coordinates, and anisotropic displacement parameters. The axial compressibility of Fe10-Al14-Bgm behaves a trend of *a* > *c* > *b*. Single-crystal refinements show that our sample contains ~6.5 mol% Fe³⁺, 3.5 mol% Fe²⁺, and 3 mol%

Al³⁺ in the large pseudo-dodecahedral site (A site), and ~11 mol% Al³⁺ in the small octahedral site (B site). This suggests that Al³⁺ preferentially occupies the B site and the excess Al³⁺ together with Fe ions stay in the A site in (Al,Fe)-bearing bridgmanite. Our results show that the primary pressure response of Fe10-Al14-Bgm structure is the compression of AO₈ polyhedra and BO₆ octahedra with monotonical decreases in A-O and B-O bonds. Further calculations indicate that the interatomic angles of B-O1-B and B-O2-B decrease from 145.2-145.8° at 4.2 GPa to 143.3-143.5° at 64.6 GPa. Quantitative analyses on two distortion-related parameters, the observed tolerance factor (t_{obs}) and octahedral tilting angles (Φ), show that t_{obs} decreases and Φ increases smoothly with pressure. These results indicate an increased distortion of the Fe10-Al14-Bgm structure with pressure, which might be related to the distortion of A-site Fe²⁺. The local environmental changes of A-site Fe²⁺ in bridgmanite could help explain previous results on the hyperfine parameters, abnormal lattice thermal conductivity, mean force constant of iron bonds and other physical properties, which in turn provide insights into our understanding on the geophysics and geochemistry of the planet.

- Keywords: (Al,Fe)-bearing bridgmanite, crystal structure, single-crystal X-ray diffraction,
- 40 lower mantle, high pressure

INTRODUCTION

Bridgmanite, (Mg,Fe)(Si,Al)O₃, is believed to be the most abundant mineral in the lower mantle, ranging from 75 to 90 vol% (Irifune et al., 2010; Murakami et al., 2012; Ringwood, 1975). Under the lower-mantle P-T conditions, bridgmanite has an orthorhombic structure with a space group of *Pbnm* (Liu, 1974). Extensive experimental studies have shown that about 10 mol% Fe and Al could be incorporated into the structure of bridgmanite in the lower mantle via two crystallographic occupancy sites: the large pseudo-dodecahedral Mg²⁺ site (A site) and the small octahedral Si⁴⁺ site (B site) (Horiuchi et al., 1987; Irifune et al., 2010; Lin et al., 2016;

Ringwood, 1975). Current consensus is that Fe^{3+} can occupy both A and B sites, while Fe^{2+} will only exist in A site (Hirose et al., 2017; Lin et al., 2013; Shukla and Wentzcovitch, 2016). However, the incorporation of Al^{3+} into bridgmanite further complicates the site occupancy and studies suggested a charge-coupled substitution of $Mg_A^{2+} + Si_B^{4+} \leftrightarrow Fe_A^{3+} + Al_B^{3+}$, where Al^{3+} replaces Si^{4+} to occupy the B site and Fe^{3+} enters the A site (e.g., Huang et al., 2021; Hummer and Fei, 2012; Lin et al., 2016). Due to the compositional and structural complexities as well as Fe valence states, direct experimental refinements on atomic structures of (Al,Fe)-bearing bridgmanite with a composition relevant to the lower-mantle mineralogical model at high pressure are still rare.

49

50

51

52

53

54

55

56

57

58

59

60

61

62

63

64

65

66

67

68

69

70

71

72

73

The technical development of miniature diamond anvil cells (DACs) with a large optical opening (above 70°) coupled with synchrotron single-crystal X-ray diffraction(SCXRD) method (Boehler, 2006; Kantor et al., 2012) allows some studies to resolve the high-pressure structure of bridgmanite (Dubrovinsky et al., 2010; Fiquet and Reynard, 1999; Ismailova et al., 2016; Ross et al., 1990; Sugahara et al., 2006; Vanpeteghem et al., 2006). Pure MgSiO₃ bridgmanite end member has shown to experience an increased structure distortion with pressure up to 15 GPa at 300 K (Ross et al., 1990; Sugahara et al., 2006). Furthermore, Dubrovinsky et al. (2010) examined the crystal structure of single-crystal (Al,Fe)-rich bridgmanite, (Mg_{0.62}Fe_{0.38})(Al_{0.36}Si_{0.64})O₃ (Fe₃₈-Al₃₆-Bgm), up to 84.1 GPa at room temperature, suggesting that the enrichment of Fe and Al in bridgmanite would greatly increase its unit-cell lattices as well as the degree of distortion. Ismailova et al. (2016) reported the synthesis of single-crystal Mg_{0.83}Fe_{0.17}Al_{0.06}Si_{0.94}O₃ (Fe₁₇-Al₆-Bgm), Mg_{0.86}Fe_{0.14}Al_{0.04}Si_{0.96}O₃ (Fe₁₄-Al₄-Bgm), and Fe²⁺_{0.64}Fe³⁺_{0.24}SiO₃ bridgmanite as well as crystal structure refinements up to 130 GPa. Considering the relevant pressure-temperature and compositional (P-T-X) conditions in the lower mantle (23-130 GPa, 1800-2500 K, and ~10 mol% Fe and Al in bridgmanite) (Irifune et al., 2010; Katsura et al., 2010; Ringwood, 1975),

it is thus critical to investigate the single-crystal structures of bridgmanite with a lower-mantle relevant composition. However, the quantitative understanding of the Fe and Al effects of the atomic structures of bridgmanite with a composition relevant to the lower mantle requires high-quality single crystals for the high-pressure structural refinements which are still lacking.

74

75

76

77

78

79

80

81

82

83

84

85

86

87

88

89

90

91

92

93

94

95

96

97

98

Experimental and theoretical studies have indicated that Fe ions, potentially occupying A and B crystallographic sites of bridgmanite, can have different electronic spin and valence states at high pressure, which can affect its chemical and physical properties (Catalli et al., 2011; Catalli et al., 2010; Dorfman et al., 2015; Hsu et al., 2011; Hsu et al., 2010; Hsu et al., 2012; Lin et al., 2008; Mao et al., 2017; Shukla et al., 2016; Tsuchiya and Wang, 2013). For instance, the B-site Fe³⁺ in bridgmanite is shown to undergo a high-spin to low-spin transition at 40-60 GPa, which is associated with an abrupt volume collapse and a drastic softening in compressional wave velocity (Catalli et al., 2011; Catalli et al., 2010; Fu et al., 2018; Hsu et al., 2011; Lin et al., 2012; Mao et al., 2015; Shukla et al., 2016). In contrast, both Fe²⁺ and Fe³⁺ in the A-site remain in the high-spin state throughout the lower-mantle pressure (Dorfman et al., 2015; Hsu et al., 2010; Li et al., 2004; Lin et al., 2016; Shukla et al., 2015). In contrast to the A-site Fe³⁺, the A-site Fe²⁺ in Fe-bearing bridgmanite displays extremely high quadrupole splitting (QS) at pressures above ~20 GPa, which has been attributed to the local site distortion (Hsu et al., 2011; Hsu et al., 2010; Jackson et al., 2005; Mao et al., 2017). Some earlier studies using X-ray emission and Mossbauer results suggested the occurrence of the intermediate-spin state in the A-site Fe²⁺ (Lin et al., 2008; McCammon et al., 2010; Narygina et al., 2010), but the high QS value of the A-site Fe²⁺ was theoretically suggested to result from the lattice distortion (Hsu et al., 2011).

The changes in the A site configuration can not only influence the aforementioned hyperfine parameters, but also other physical properties of bridgmanite at high pressure. For instance, Yang et al. (2019) found a drastic softening of 21% in mean force constants of iron

bonds in Fe-bearing and (Al,Fe)-bearing bridgmanite at 40-60 GPa from nuclear resonant inelastic X-ray scattering measurements, which is attributed to the effect of the A-site distortion from low to high QS states. In addition, a recent study measured lattice thermal conductivity of bridgmanite up to 120 GPa at room temperature using laser pump-probe spectroscopy (Hsieh et al., 2017). The observed 20% drop of thermal conductivity in Fe-bearing bridgmanite at ~45 GPa could possibly result from the pressure-induced distortion of the A-site Fe²⁺ (Hsieh et al., 2017). However, atomistic scale evidence for these macroscopic-scale observations remains limited. Further quantitative analyses on the atomistic structure of (Al,Fe)-bearing bridgmanite, such as site occupancies of Fe ions and Al³⁺ and atomic coordinates, are required to provide insights into the physical properties of bridgmanite and to model lower-mantle geophysics and geodynamics (Garnero et al., 2007; Lin et al., 2013; Mao et al., 2017; Masters et al., 2000).

In this study, we have carried out SCXRD experiments on (Al,Fe)-bearing bridgmanite, (Mg0.88Fe³⁺0.065Fe²⁺0.035Al0.03)(Al0.11Si0.90)O3 (Fe10-Al14-Bgm), up to 64.6 GPa using a Boehler-Almax type DAC with synchrotron radiations. The use of two crystal platelets allows us to collect up to 230-300 reflection peaks with intensities (I) of $I > 3\sigma(I)$ at each experimental pressure to derive its high-pressure lattice parameters and atomic coordinates. These data are analyzed to help understand site occupancies of Fe²⁺, Fe³⁺, and Al³⁺ in Fe10-Al14-Bgm as well as to determine its high-pressure structural variations, including bond lengths and angles, octahedral titling, and degree of lattice distortion. These results could provide important clues for understanding the effect of local iron environment on the physical and chemical properties of bridgmanite.

EXPERIMENTAL DETAILS

High-quality (Al,Fe)-bearing bridgmanite was synthesized at ~24 GPa and ~1800 °C for 20 h in the presence of hydrous melt using the 5000-ton Kawai-type multi-anvil apparatus with

a run number of 5K2667 at the Institute for Planetary Materials at Okayama University. Details of sample synthesis and characterizations have been well documented in early studies (Fu et al., 2019; Fu et al., 2022). Further electron microprobe analysis and Mössbauer spectroscopy results show that the synthesized bridgmanite has a homogenous composition of Mg_{0.88}Fe_{0.1}Al_{0.14}Si_{0.90}O₃ (Fe₁0-Al₁₄-Bgm) with Fe³⁺/ Σ Fe=~0.65 (Fu et al., 2019). Synchrotron XRD results on the sample show sharp diffraction spots with lattice parameters of a = 4.7875(3) Å, b = 4.9423(2) Å, c = 6.9205(6) at ambient conditions in a *Pbnm* space group, confirming its high quality for SCXRD experiments (Figure 1).

123

124

125

126

127

128

129

130

131

132

133

134

135

136

137

138

139

140

141

142

143

144

145

146

147

A short symmetric DAC equipped with a pair of 250-µm Boehler-Almax type anvils was used for high-pressure SCXRD experiments (Boehler, 2006). One anvil glued onto a cubic boron nitride (cBN) seat was used to face the upstream incident beam while the other anvil glued onto a tungsten-carbide seat with a large opening angle up to 70° (40) was used as the downstream side for diffraction collections. The upstream cBN seat absorbs a noticeable degree of X-rays and avoids producing powder diffraction signals from the backing plate (Dera et al., 2013). A 250-μm thick Re gasket was pre-indented to ~25 GPa or 25-30 μm thickness, and a hole with a diameter of 150 µm was drilled in the pre-indented area to be used as a sample chamber. Knowing that each bridgmanite platelet in the DAC can only give rise to certain parts of the reciprocal space of the crystal lattice, the use of several crystal platelets in different crystallographic orientations in single-crystal DAC experiments is highly desirable for collections of more reflection spots and thus better statistics in the structural refinements (Ross et al., 1990). Here, we double-side polished two random orientations of bridgmanite platelets that were $\sim 20 \,\mu\text{m} \times 20 \,\mu\text{m}$ big and $\sim 5-7 \,\mu\text{m}$ thick. These two clean platelets were loaded into the sample chamber, together with a piece of Au as pressure calibrant (Figure 1c insert). The Au and two bridgmanite platelets were intentionally placed as a triangular geometry to minimize pressure differences in the sample chamber during high-pressure experiments. Neon was loaded into the sample chamber as a pressure medium using a gas loading system in the Mineral Physics Laboratory of the Department of Geological Sciences at the University of Texas at Austin.

148

149

150

151

152

153

154

155

156

157

158

159

160

161

162

163

164

165

166

167

168

169

In situ high-pressure synchrotron SCXRD experiments were performed on Fe10-Al14-Bgm up to 64.6 GPa with a pressure interval of ~3 GPa at the beamline 13ID-D GeoSoilEnviroCARS (GSECARS) of the Advanced Photon Source (APS), Argonne National Laboratory. An incident X-ray beam with an energy of 42 keV and a wavelength of 0.2952 Å was focused to a beam size of approximately 3 µm × 3 µm on the sample. Single-crystal XRD step-scan measurements were conducted on each platelet by rotating $\pm 30^{\circ}$ of the DAC about the vertical axis of the sample stage with a step size of 0.5° and an exposure time of 1 or 2 s/step. A total of 120 XRD frames were collected for each platelet by a Pilatus 1M CdTe detector at each experimental pressure. Pressures and pressure uncertainties were determined by measuring the unit-cell volume of Au right before and after each SCXRD measurement (Fei et al., 2007). These single-crystal patterns were processed for data reduction using the CrysAlisPro software (Diffraction, 2019). This procedure enables us to determine the lattice parameters, extract the intensity of each hkl reflection, and perform absorption corrections. Single-crystal refinements on the high-pressure atomic structure of Fe10-14-Bgm were further carried out on the combined reflection datasets of two platelets by using the JANA software (Petříček et al., 2014). These structure refinements eventually resolve atomic coordinates and anisotropic displacement parameters of each atom in the sample (Table 1, supporting information cif files). Residual R-factor (R and wR in %) were used to evaluate the quality of the refinement, defined as:

$$R(\%) = \left[\frac{\sum |F_o^2 - F_c^2|}{\sum w F_o^2} \right]^{1/2} \times 100$$
 (1)

$$wR(\%) = \left[\frac{\sum w |F_o^2 - F_c^2|}{\sum w F_o^2} \right]^{1/2} \times 100$$
 (2)

where F_o and F_c are observed and calculated structure factor amplitudes, respectively, and w is a weighting factor (Figure 2 and Table 1). We used the VESTA software to view and graph the refined crystal structure of Fe10-Al14-Bgm at high pressure (Momma and Izumi, 2011).

RESULTS AND DATA ANALYSES

Figure 1 shows representative raw SCXRD patterns of both platelets ($\pm 30^{\circ}$) at ~ 52.7 GPa. The circular and round diffraction spots with an average FWHM of 0.07° - 0.10° confirm the high-quality of our single-crystal Fe10-Al14-Bgm without apparent development of cleavage or texture at high pressure with neon as a transmitting pressure medium. Our individual analyses on the total 120 XRD frames of each platelet using the CrysAlisPro software (Diffraction, 2019) show that both loaded platelets have high-quality reflections (Figure 2a) and similar unit-cell parameters (< 0.2%) at each experimental pressure. The obtained lattice parameters (a, b, c) and unit-cell volume (V) of Fe10-Al14-Bgm decrease monotonically with pressure up to 64.6(6) GPa (Table 1 and Figure 3). Third-order Birch-Murnaghan equation of state (EoS) is used to evaluate the high-pressure axial and bulk incompressibility of Fe10-Al14-Bgm. The best fits to pressure-volume (P-V) data yield $K_{T0} = 256 \pm 2$ GPa, $K'_{T0} = 4$ (fixed), or $K_{T0} = 259 \pm 4$ GPa, $K'_{T0} = 3.8 \pm 0.2$, with a fixed V_0 of 163.75(3) Å 3 .

Refinements were conducted to resolve the structure of single-crystal Fe10-Al14-Bgm by initially setting the atomic coordinates of A-site, B-site, O1, and O2 atoms as those of MgSiO₃ bridgmanite (space group: *Pbnm*) (Horiuchi et al., 1987). The total abundances of Mg²⁺, Si⁴⁺, Al³⁺, Fe ions were fixed from the EPMA results, and the relative ratio of Fe²⁺ and Fe³⁺ was obtained from Mössbauer measurements on the same sample (Fu et al., 2019). Regarding the site occupancy of different ions, we fixed 88 mol% Mg²⁺ and 90 mol% Si⁴⁺ in the A and B

sites, respectively, and we considered that Fe ions and Al³⁺ can stay in both A and B sites. The refinement process assumes the same atomic coordinates for ions in the same site and the software does not distinguish Fe ions between Fe²⁺ and Fe³⁺. It should be noted that theoretical calculations have suggested the atomic positions of different Fe²⁺ and Fe³⁺ components in the same site are similar and indistinguishable in bridgmanite (Hsu et al., 2011; Hsu et al., 2010), supporting the aforementioned assumptions in the structure refinements using the JANA software (Petříček et al., 2014).

During the refinement, we relaxed the following parameters, including abundances of Fe ions and Al³⁺ in both A and B sites, atomic coordinates of each site and anisotropic displacement parameters of each atom. The best fits to combined reflection peaks of the two platelets show that our (Al,Fe)-bearing bridgmanite sample has a chemical composition of (Mg_{0.88}Fe³⁺_{0.065}Fe²⁺_{0.035}Al_{0.03})(Al_{0.11}Si_{0.90})O₃ with all the Fe ions and ~3 mol% Al³⁺ in the A site and ~11 mol% Al³⁺ in the B site. The residual *R*-factors, wR, is about 3.2% at the initial pressure of 4.2(1) GPa (Figure 2b), indicating reliable constraints on the structure of single-crystal Fe₁0-Al₁4-Bgm (Toby, 2006). Although the number of diffraction peaks decreases with increasing pressure, the use of two platelets allows over 230 peaks with $I > 3\sigma(I)$ for the structure refinements even at the highest experimental pressure of 64.6(6) GPa. The low *R* and wR values indicate small uncertainties of our refinements (Figure 2 and Table 1). We conducted several synthetic tests to fix a certain amount of Fe ions in the B site, however, the resultant wR is unreasonably high, >20%, even at 4.2(1) GPa. These tests rule out the possibility of Fe ions occupying the B site within uncertainties of the structure refinements.

DISCUSSION

Lattice parameters of (Al,Fe)-bearing bridgmanite at high pressure

Compared with literature reports on bridgmanite with different Fe and Al contents, the unitcell Fe10-Al14-Bgm comparable of parameters of are those $Mg_{0.89}Fe^{2+}_{0.024}Fe^{3+}_{0.096}Al_{0.11}Si_{0.89}O_3$ (Fe12-Al11-Bgm) (Mao et al., 2017), slightly greater than those of pure MgSiO₃ bridgmanite end member (Boffa Ballaran et al., 2012), and much lower than those of (Al,Fe)-rich bridgmanite, $(Mg_{0.60}Fe^{2+}_{0.03}Fe^{3+}_{0.38})(Al_{0.36}Si_{0.62})O_3$ (Fe41-Al36-Bgm) (Boffa Ballaran et al., 2012), Fe38-Al36-Bgm (Dubrovinsky et al., 2010), and Fe²⁺_{0.64}Fe³⁺_{0.24}SiO₃ bridgmanite (Ismailova et al., 2016) (Figure 3a-c). This indicates that incorporation of Fe and Al into bridgmanite significantly increases its unit-cell lattice parameters mainly due to the larger size of Fe ions compared to Mg²⁺ and Si⁴⁺. In addition, our analyses show that the axial compressibility of Fe10-Al14-Bgm shows a trend of a > c > b(Figure 3d-f), consistent with those of MgSiO₃ and Fe²⁺_{0.64}Fe³⁺_{0.24}SiO₃ bridgmanite end members (Boffa Ballaran et al., 2012; Ismailova et al., 2016). In contrast, Boffa Ballaran et al. (2012) reported that c axis of Fe41-Al36-Bgm is the most compressible axis, suggesting that intermediate Fe and Al in bridgmanite may change the direction of the maximum axial compressibility. Additionally, early studies reported noticeable volume collapses of 0.5-0.8% in pure Fe-bearing bridgmanite at 40-60 GPa (Fu et al., 2018; Mao et al., 2015) because of the spin transition of B-site Fe³⁺. Our Fe10-Al14-Bgm does not display apparent volume collapses, supporting our refinements on the site occupancies that all Fe ions stay in the A site (without any observable B-site Fe³⁺) and remain in the high-spin state up to 64.6(6) GPa. These results are also consistent with early theoretical modeling on the spin and valences of the A-site and B-site Fe ions in bridgmanite and their effects on unit-cell volumes (Hsu et al., 2011; Hsu et al., 2010; Shukla et al., 2016).

215

216

217

218

219

220

221

222

223

224

225

226

227

228

229

230

231

232

233

234

235

236

237

238

239

Bond lengths and angles in (Al,Fe)-bearing bridgmanite at high pressure

The obtained atomic coordinates of Fe10-Al14-Bgm can be used to precisely determine its structural response to compression, such as interatomic distances and bond angles among atoms

(Table 2). For an ideal perovskite structure, the A and B sites will have twelvefold and sixfold coordination to form AO₁₂ dodecahedra and BO₆ octahedra, respectively. Kudoh et al. (1987) observed that in MgSiO₃ bridgmanite, the application of pressure up to 9.6 GPa changes the A-site polyhedral configuration towards eightfold coordination (AO₈ polyhedron) rather than twelvefold coordination. Each AO₈ polyhedron shares two faces, four edges, and two corners with the eight surrounding BO₆ octahedra. Here we calculated mean interatomic distances between A-site (B-site) atoms and O within an eight (six) coordination, denoted as <A-O>8 (<B-O>), using the derived high-pressure atomic coordinates (Figures 4 and 5a). The average interatomic distances between A-site cations and O within an AO₁₂ pseudo-dodecahedron (<A-O>12) were also calculated for comparison. Results show that <A-O>8, <A-O>12, and <B-O> of the single-crystal Fe10-Al14-Bgm decrease smoothly with pressure from 2.192(1), 2.471(1), and 1.795(1) Å, respectively at 4.2(1) GPa to 2.052(5), 2.347(5), and 1.715(3) Å, respectively at 64.6(6) GPa. Furthermore, variations of bond lengths in the BO₆ octahedra decrease with pressure, suggesting the BO₆ octahedra is approaching to form an ideal octahedra at high pressure (Figure 4). Comparisons with literature data on bridgmanite with different compositions (Dubrovinsky et al., 2010; Ross et al., 1990; Sugahara et al., 2006) show that incorporation of 36 mol% Al and 38 mol% Fe into its structure will increase <B-O> and <A-O>12 by approximately 2.1% and 1.7%, respectively, but affects <A-O>8 little, less than 0.5%. That is, the incorporation of Fe and Al into bridgmanite has a stronger effect on the BO₆ octahedron than the AO₈ polyhedron.

240

241

242

243

244

245

246

247

248

249

250

251

252

253

254

255

256

257

258

259

260

261

262

263

264

We have also calculated two angles between O and B-site atoms, B-O1-B and B-O2-B, which have been served as helpful indicators on the tilting of the BO₆ octahedra (Andrault and Poirier, 1991). Specifically, the B-O1-B and B-O2-B represent the tilting of the BO₆ octahedra in the *b-c* plane and the *a-b* plane, respectively. Calculations show that B-O1-B and B-O2-B of Fe10-Al14-Bgm are about 145.2(2)° and 145.8(2)°, respectively, at 4.2(1) GPa, which

gradually decrease to about 143.3(3)° and 143.5(3)°, respectively, at 64.6(6) GPa (Figure 5b-c). This indicates an increasing tilt of the BO₆ octahedra with pressure. The pressure effect on tilting angles of the BO₆ octahedra in both *b-c* and *a-b* planes in Fe10-Al14-Bgm is consistent with those of Fe38-Al35-Bgm (Dubrovinsky et al., 2010) and pure MgSiO₃ bridgmanite end member (Sugahara et al., 2006). Furthermore, we have noticed that with increasing Fe and Al contents from Fe10-Al14-Bgm to Fe38-Al36-Bgm in bridgmanite, both angles of B-O1-B and B-O2-B decrease 1.4-1.6%, showing a strong Fe and Al incorporation effect on the distortion of the BO₆ octahedra.

Structural distortion of (Al,Fe)-bearing bridgmanite at high pressure

To quantitatively evaluate the distortion of the bridgmanite structure in the lower-mantle pressure, we followed literature procedures to calculate two relevant parameters, the observed tolerance factor (t_{obs}) and octahedral tilting angles (Φ), using the refined atomic structure of Fe10-Al14-Bgm from a microscopic approach (Ross et al., 1990; Sugahara et al., 2006; Zhao et al., 1993a). The t_{obs} is initially used to systematically describe the tilting and distortion in GdFeO₃-type perovskite (Sasaki et al., 1983), calculated as:

$$t_{obs} = \frac{\langle A - 0 \rangle_{12}}{\langle B - 0 \rangle} \tag{3}$$

where $\langle A - O \rangle_{12}$ ($\langle B - O \rangle$) is the mean interatomic distance between A-site (B-site) atoms and O within a twelvefold (sixfold) coordination. According to the definition, an ideal cubic GdFeO₃ perovskite will have $t_{\rm obs}$ as one. Our calculations show that the $t_{\rm obs}$ of Fe10-Al14-Bgm is about 0.974(1) at 4.2(1) GPa and decreases with pressure to \sim 0.968(4) at 64.6(6) GPa (Figure 6). Thus, there is an increasing degree of the lattice distortion in Fe10-Al14-Bgm from an ideal cubic symmetry in the orthorhombic system with pressure. In addition, compared to literature reports on bridgmanite with different compositions, the $t_{\rm obs}$ of Fe10-Al14-Bgm is slightly lower than those of MgSiO₃ end member (Ross et al., 1990; Sugahara et al., 2006) and higher than

those of Fe38-Al35-Bgm (Dubrovinsky et al., 2010), suggesting an increased structure distortion in (Al,Fe)-rich bridgmanite.

Taking advantage of the obtained atomic coordinates of the single-crystal Fe10-Al14-Bgm in this study, we can reliably calculate the titling angles of the octahedron (Φ) to describe the distortion degree of bridgmanite at high pressure. In this method, the octahedron in the structure of bridgmanite is assumed as a pseudo-cubic unit cell with a length (a_p) approximately described as: $a_p \approx \sqrt{2}a/2 \approx \sqrt{2}b/2 \approx c/2$ (Figure 7a). Φ is defined as titling of the octahedron about the pseudo-cubic [111] direction. Alternatively, Φ can be viewed as a combination of titling about the pseudo-cubic [110] direction (angle θ) and the pseudo-cubic [001] direction (angle φ) in the pseudo-cubic unit cell (Figure 7b), calculated using:

$$\cos \Phi = \cos \theta \cos \varphi \tag{4}$$

$$\tan \theta = 4\sqrt{u_{01}^2 + v_{01}^2/c} \tag{5}$$

$$\tan \varphi = 4\sqrt{u_{02}^2 + v_{02}^2} / \sqrt{a^2 + b^2} \tag{6}$$

where u_{01} , u_{02} , v_{01} , and v_{02} are parameters derived from refined atomic coordinates using:

$$u_{01} = ax_{01} (7)$$

$$v_{01} = b(0.5 - y_{01}) \tag{8}$$

$$u_{02} = a(0.25 - x_{02}) \tag{9}$$

$$v_{02} = b(y_{02} - 0.25) (10)$$

where x_{On} and y_{On} are atomic coordinates of the *n*th oxygen atom (Zhao et al., 1993a). Calculations show that Φ of Fe10-Al14-Bgm gradually increases with pressure from ~21.0(1)° at 4.2(1) GPa to ~22.5(3)° at 64.6(6) GPa (Figure 8), indicating an increasing distortion.

Comparison with literature results suggests that Φ of bridgmanite also increases with increasing Fe and Al contents (Dubrovinsky et al., 2010; Ross et al., 1990; Sugahara et al., 2006). We note that, due to the experimental difficulties in obtaining reliable high-pressure atomic structure of bridgmanite, some early studies attempted to estimate the value of Φ from its unit-cell parameters in a macroscopic approach by assuming regular octahedra in the structure, calculated as: $\cos \Phi = \sqrt{2}\alpha^2/bc$ (Mao et al., 2017; O'keeffe et al., 1977). Comparisons of the calculated Φ from both macroscopic and microscopic approaches (Boffa Ballaran et al., 2012; Mao et al., 2017) show that the macroscopic approach typically underestimates Φ (Figure 8). This is due to the fact that the macroscopic approach simply assumes that the octahedron in bridgmanite is rigid and the octahedral angles are small (Zhao et al., 1993a; Zhao et al., 1993b).

The calculated $t_{\rm obs}$ and Φ show a consistent trend that the distortion degree of the Fe10-Al14-Bgm structure increases with pressure (Figures 6 and 8). Our SCXRD refinements reveal that all the Fe ions in our Fe10-Al14-Bgm, about 6.5 mol% Fe³⁺ and 3.5 mol% Fe²⁺, occupy the A site within uncertainties of the refinements. Therefore, the observed high-pressure distortion in Fe10-Al14-Bgm should be closely related to changes of local A-site Fe ions environment. Both earlier theoretical and experimental studies indicate that the A-site Fe²⁺ and Fe³⁺ remain in the high-spin state throughout the lower-mantle pressure, and the A-site Fe²⁺ can experience an enhanced distortion at 40-60 GPa with extremely high QS (Hsu et al., 2011; Hsu et al., 2010; Mao et al., 2017). Theoretical calculations also show that the small changes in the local structure and *d*-orbital occupations of Fe²⁺ in bridgmanite can greatly affect its QS (Bengtson et al., 2009; Hsu et al., 2010). Therefore, we attribute the increased SiO₆ octahedron tilting angles and distortion degree in Fe10-Al14-Bgm to the increased distortion of the A-site Fe²⁺ at high pressures. These local changes of A-site Fe²⁺ environment in bridgmanite can result in high QS values as observed experimentally (Jackson et al., 2005; Mao et al., 2017).

We note that the abundance of Fe³⁺ in our Fe10-Al14-Bgm is much higher than that of Fe²⁺, which might weaken the distortion degree of A-site Fe²⁺ and result in smooth increase in $t_{\rm obs}$ and Φ with pressure. Moreover, Mao et al. (2017) observed the existence of both high and low QS A-site Fe²⁺ components in the Fe12-Al11-Bgm at 0-130 GPa and suggest that the presence of Al may play a key role in decreasing the differences between high and low QS A-site Fe²⁺.

IMPLICATIONS

Approximately 5-7 wt% Al₂O₃ can be dissolved into (Al,Fe)-bearing bridgmanite via the decomposition of majoritic garnet at the topmost lower mantle (~660-770 km in depth) (Hummer and Fei, 2012; Irifune et al., 2010; Lin et al., 2016). Our refined crystal structure of the Fe10-Al14-Bgm suggests that Al³⁺ would preferentially occupy the B site and all the Fe ions stay in the A site in (Al,Fe)-bearing bridgmanite. That is, the lower-mantle (Al,Fe)-bearing bridgmanite is not expected to contain the B-site Fe³⁺, and thus, will not experience the B-site spin transition as well as the associated thermoelastic anomalies as discussed in the previous reports (Fu et al., 2018; Hsu et al., 2011; Mao et al., 2015; Shukla et al., 2016).

Studies have shown that the enhanced distortion of A-site Fe²⁺ in bridgmanite does not cause detectable anomalies in unit-cell volumes (Boffa Ballaran et al., 2012; Mao et al., 2017) but could be linked with enhanced hyperfine parameters and softening in some macroscopic properties, such as lattice thermal conductivity and mean force constants of iron bonds (Hsieh et al., 2017; Yang et al., 2019). For instance, Hsieh et al. (2017) found that MgSiO₃, Fe-bearing Mg_{0.96}Fe_{0.07}Si_{0.98}O₃ (Fe7-Bgm), and (Al,Fe)-bearing Mg_{0.89}Fe²⁺_{0.024}Fe³⁺_{0.096}Al_{0.11}O₃ Si_{0.89}O₃ (Fe12-Al11-Bgm) have comparable and increasing lattice thermal conductivities with pressure below 40 GPa. This can be explained by the pressure-induced shortening of the interatomic distances in the bridgmanite structure (Figure 5). While the thermal conductivity of Fe7-Bgm drops by ~20% at 40-45 GPa and then changes little with further increasing pressure. Such a

drop in the conductivity is likely related to the distortion of the A-site Fe²⁺ occurring in the same pressure range. The lattice distortion can increase the phonon-defect and reduce the phonon-phonon scattering contribution in bridgmanite (Ladd et al., 1986; Schelling et al., 2002) consequently leading to the reduced lattice thermal conductivity at high pressure. Because of the trade-offs between the positive effect of shortened interatomic distances and the negative effect of the A-site Fe²⁺ distortion, the pressure dependence of the lattice thermal conductivity in Fe7-Bgm is almost flat above 45 GPa (Hsieh et al., 2017). In comparison, Fe12-Al11-Bgm displays a moderate thermal conductivity between MgSiO₃ and Fe7-Bgm above 40 GPa (Hsieh et al., 2017). Due to the relative abundance of Fe²⁺ and Fe³⁺ as well as the presence of Al³⁺ in (Al,Fe)-bearing bridgmanite, the A-site Fe2+ distortion is likely weakened, and thus, its decreasing effect on thermal conductivity will be weakened. This trend is consistent with our observations on the gradual distortion instead of abrupt anomalies with pressure in Fe10-Al14-Bgm. Similarly, the drastic softening in force constants of (Al,Fe)-bearing bridgmanite at 40-60 GPa observed by Yang et al. (2019) might be caused by the A-site Fe²⁺ distortion: the weak pressure dependence of force constants above 60 GPa is possibly a result of the combined effect between the shorten interatomic bond lengths and A-site Fe²⁺ distortion at high pressure, which has positive and negative effects on force constants, respectively. Thermal conductivity and force constants of lower-mantle candidate minerals are key for understanding geophysics and geochemistry of our planet, such as the heat flux across the core-mantle boundary and isotope fractionation in an early magma ocean (Hofmeister, 1999; Poitrasson et al., 2004). Therefore, the softening effect of the A-site Fe²⁺ distortion could greatly affect our views on mantle convection flow and evolution history of the planet. Considering that our study is limited to room temperature on (Al,Fe)-bearing bridgmanite with low A-site Fe²⁺, further examinations of the thermal effect on atomic structures of Fe²⁺-rich (Al,Fe)-bearing bridgmanite at high

351

352

353

354

355

356

357

358

359

360

361

362

363

364

365

366

367

368

369

370

371

372

373

pressure are still needed to better interpret the lower-mantle geochemistry, geophysics, and
 geodynamics.
 Acknowledgement

J.F. Lin acknowledges support from National Science Foundation Geophysics Program (EAR-1916941 & EAR-2001381) and the Joint Use/Research Program of the Institute for Planetary Materials, Okayama University. T. Okuchi acknowledges support from JSPS KAKENHI (17H01172). We appreciate N. Purevjave for her assistance on the crystal synthesis. SCXRD experiments were conducted at 13ID-D, GeoSoilEviroCARS (The University of Chicago, Sector 13), Advanced Photon Source, Argonne National Laboratory. GeoSoilEnviroCARS is supported by the National Science Foundation - Earth Sciences (EAR-1634415) and U.S. Department of Energy (DOE) Office of Science User Facility operated for the DOE office of

Data availability

All the high-pressure cif files of the single-crystal bridgmanite in this study are provided in supplementary materials.

Science by Argonne National Laboratory under Contract No. DE-AC02-06CH11357.

Competing interests

The authors declare no competing interests.

392

393

378

379

380

381

382

383

384

385

386

387

390

391

References:

- Andrault, D., and Poirier, J. (1991) Evolution of the distortion of perovskites under pressure: an EXAFS study of BaZrO₃, SrZrO₃ and CaGeO₃. Physics and Chemistry of Minerals, 18(2), 91-105.
- Bengtson, A., Li, J., and Morgan, D. (2009) Mössbauer modeling to interpret the spin state of iron in (Mg,Fe)SiO₃ perovskite. Geophysical Research Letters, 36(15).
- Boehler, R. (2006) New diamond cell for single-crystal x-ray diffraction. Review of Scientific Instruments, 77(11), 115103.

- Boffa Ballaran, T., Kurnosov, A., Glazyrin, K., Frost, D.J., Merlini, M., Hanfland, M., and Caracas, R. (2012)
 Effect of chemistry on the compressibility of silicate perovskite in the lower mantle. Earth and
 Planetary Science Letters, 333, 181-190.
- Catalli, K., Shim, S.-H., Dera, P., Prakapenka, V.B., Zhao, J., Sturhahn, W., Chow, P., Xiao, Y., Cynn, H., and Evans, W.J. (2011) Effects of the Fe ³⁺ spin transition on the properties of aluminous perovskite—New insights for lower-mantle seismic heterogeneities. Earth and Planetary Science Letters, 310(3), 293-302.
- Catalli, K., Shim, S.-H., Prakapenka, V.B., Zhao, J., Sturhahn, W., Chow, P., Xiao, Y., Liu, H., Cynn, H., and Evans, W.J. (2010) Spin state of ferric iron in MgSiO₃ perovskite and its effect on elastic properties. Earth and Planetary Science Letters, 289(1), 68-75.

411

412

415

416

417

418

419

420

421

422

423

424

425

426

427

428

429

430

431

432

433

434

435

436

- Dera, P., Zhuravlev, K., Prakapenka, V., Rivers, M.L., Finkelstein, G.J., Grubor-Urosevic, O., Tschauner, O., Clark, S.M., and Downs, R.T. (2013) High pressure single-crystal micro X-ray diffraction analysis with GSE_ADA/RSV software. High Pressure Research, 33(3), 466-484.
- Diffraction, R.O. (2019) CrysAlisPro software system, version 1.171.40.45 a; Rigaku Corporation.

 Oxford, UK.
 - Dorfman, S.M., Badro, J., Rueff, P., Chow, P., Xiao, Y., and Gillet, P. (2015) Composition dependence of spin transition in (Mg,Fe)SiO₃ bridgmanite. American Mineralogist, 100(10), 2246-2253.
 - Dubrovinsky, L., Boffa-Ballaran, T., Glazyrin, K., Kurnosov, A., Frost, D., Merlini, M., Hanfland, M., Prakapenka, V.B., Schouwink, P., and Pippinger, T.J.H.P.R. (2010) Single-crystal X-ray diffraction at megabar pressures and temperatures of thousands of degrees. 30(4), 620-633.
 - Fei, Y.W., Ricolleau, A., Frank, M., Mibe, K., Shen, G.Y., and Prakapenka, V. (2007) Toward an internally consistent pressure scale. Proceedings of the National Academy of Sciences of the United States of America, 104(22), 9182-9186.
 - Figuet, G., and Reynard, B. (1999) High-pressure equation of state of magnesite: New data and a reappraisal. American Mineralogist, 84(5-6), 856-860.
 - Fu, S., Yang, J., Karato, S.i., Vasiliev, A., Presniakov, M.Y., Gavrilliuk, A.G., Ivanova, A.G., Hauri, E.H., Okuchi, T., and Purevjav, N. (2019) Water concentration in single-crystal (Al, Fe)-bearing bridgmanite grown from the hydrous melt: implications for dehydration melting at the topmost lower mantle. Geophysical Research Letters.
 - Fu, S., Yang, J., Zhang, Y., Okuchi, T., McCammon, C., Kim, H.I., Lee, S.K., and Lin, J.F. (2018) Abnormal Elasticity of Fe Bearing Bridgmanite in the Earth's Lower Mantle. Geophysical Research Letters, 45(10), 4725-4732.
 - Fu, S., Zhang, Y., Okuchi, T., and Lin, J.-F. (2022, in production) Single-crystal elasticity of (Al,Fe)-bearing bridgmanite up to 82 GPa. American Mineralogist, https://doi.org/10.2138/am-2022-8435.
 - Garnero, E.J., Lay, T., and McNamara, A. (2007) Implications of lower-mantle structural heterogeneity for the existence and nature of whole-mantle plumes. Geological Society of America Special Papers, 430, 79-101.
- Hirose, K., Sinmyo, R., and Hernlund, J. (2017) Perovskite in Earth's deep interior. Science, 358(6364), 734-738.
- Hofmeister, A. (1999) Mantle values of thermal conductivity and the geotherm from phonon lifetimes.
 Science, 283(5408), 1699-1706.
 Horiuchi, H., Ito, E., and Weidner, D.J. (1987) Perovskite-type MgSiO₃: single-crystal X-ray diffraction
 - Horiuchi, H., Ito, E., and Weidner, D.J. (1987) Perovskite-type MgSiO₃: single-crystal X-ray diffraction study. American Mineralogist, 72(3-4), 357-360.
- Hsieh, W.P., Deschamps, F., Okuchi, T., and Lin, J.F. (2017) Reduced lattice thermal conductivity of Febearing bridgmanite in Earth's deep mantle. Journal of Geophysical Research: Solid Earth.
- Hsu, H., Blaha, P., Cococcioni, M., and Wentzcovitch, R.M. (2011) Spin-state crossover and hyperfine interactions of ferric iron in MgSiO 3 perovskite. Physical Review Letters, 106(11), 118501.
- Hsu, H., Umemoto, K., Blaha, P., and Wentzcovitch, R.M. (2010) Spin states and hyperfine interactions of iron in (Mg,Fe) SiO₃ perovskite under pressure. Earth and Planetary Science Letters, 294(1), 19-26.

- Hsu, H., Yonggang, G.Y., and Wentzcovitch, R.M. (2012) Spin crossover of iron in aluminous MgSiO₃ perovskite and post-perovskite. Earth and Planetary Science Letters, 359, 34-39.
- Huang, R., Boffa Ballaran, T., McCammon, C.A., Miyajima, N., and Frost, D.J. (2021) The Effect of Fe-Al Substitution on the Crystal Structure of MgSiO₃ Bridgmanite. Journal of Geophysical Research: Solid Earth, 126(9), e2021JB021936.
- Hummer, D.R., and Fei, Y. (2012) Synthesis and crystal chemistry of Fe³⁺-bearing (Mg,Fe³⁺)(Si, Fe³⁺)O₃
 perovskite. American Mineralogist, 97(11-12), 1915-1921.
- 457 Irifune, T., Shinmei, T., McCammon, C.A., Miyajima, N., Rubie, D.C., and Frost, D.J. (2010) Iron 458 partitioning and density changes of pyrolite in Earth's lower mantle. Science, 327(5962), 193-459 195.

461

462

463

464

465

466 467

468

469

470

471 472

473

474

475

476

477

478

479

480

481

482

483

484

485

- Ismailova, L., Bykova, E., Bykov, M., Cerantola, V., McCammon, C., Ballaran, T.B., Bobrov, A., Sinmyo, R., Dubrovinskaia, N., and Glazyrin, K. (2016) Stability of Fe, Al-bearing bridgmanite in the lower mantle and synthesis of pure Fe-bridgmanite. Science Advances, 2(7), e1600427.
- Jackson, J.M., Sturhahn, W., Shen, G., Zhao, J., Hu, M.Y., Errandonea, D., Bass, J.D., and Fei, Y. (2005)
 A synchrotron Mössbauer spectroscopy study of (Mg,Fe)SiO₃ perovskite up to 120 GPa.
 American Mineralogist, 90(1), 199-205.
- Kantor, I., Prakapenka, V., Kantor, A., Dera, P., Kurnosov, A., Sinogeikin, S., Dubrovinskaia, N., and Dubrovinsky, L. (2012) BX90: A new diamond anvil cell design for X-ray diffraction and optical measurements. Review of Scientific Instruments, 83(12), 125102.
- Katsura, T., Yoneda, A., Yamazaki, D., Yoshino, T., and Ito, E. (2010) Adiabatic temperature profile in the mantle. Physics of the Earth and Planetary Interiors, 183(1-2), 212-218.
- Kudoh, Y., Ito, E., and Takeda, H. (1987) Effect of pressure on the crystal structure of perovskite-type MgSiO₃. Physics and Chemistry of Minerals, 14(4), 350-354.
- Ladd, A.J., Moran, B., and Hoover, W.G. (1986) Lattice thermal conductivity: A comparison of molecular dynamics and anharmonic lattice dynamics. Physical Review B, 34(8), 5058.
- Li, J., Struzhkin, V.V., Mao, H.-k., Shu, J., Hemley, R.J., Fei, Y., Mysen, B., Dera, P., Prakapenka, V., and Shen, G. (2004) Electronic spin state of iron in lower mantle perovskite. Proceedings of the National Academy of Sciences of the United States of America, 101(39), 14027-14030.
- Lin, J.-F., Alp, E.E., Mao, Z., Inoue, T., McCammon, C., Xiao, Y., Chow, P., and Zhao, J. (2012) Electronic spin states of ferric and ferrous iron in the lower-mantle silicate perovskite. American Mineralogist, 97(4), 592-597.
- Lin, J.F., Mao, Z., Yang, J., Liu, J., Xiao, Y.M., Chow, P., and Okuchi, T. (2016) High-spin Fe²⁺ and Fe³⁺ in single-crystal aluminous bridgmanite in the lower mantle. Geophysical Research Letters, 43(13), 6952-6959.
- Lin, J.F., Speziale, S., Mao, Z., and Marquardt, H. (2013) Effects of the Electronic Spin Transitions of Iron in Lower Mantle Minerals: Implications for Deep Mantle Geophysics and Geochemistry. Reviews of Geophysics, 51(2), 244-275.
- Lin, J.F., Watson, H., Vanko, G., Alp, E.E., Prakapenka, V.B., Dera, P., Struzhkin, V.V., Kubo, A., Zhao, J.Y., McCammon, C., and Evans, W.J. (2008) Intermediate-spin ferrous iron in lowermost mantle post-perovskite and perovskite. Nature Geoscience, 1(10), 688-691.
- 490 Liu, L.g. (1974) Silicate perovskite from phase transformations of pyrope-garnet at high pressure and 491 temperature. Geophysical Research Letters, 1(6), 277-280.
- Mao, Z., Lin, J.F., Yang, J., Inoue, T., and Prakapenka, V.B. (2015) Effects of the Fe³⁺ spin transition on the equation of state of bridgmanite. Geophysical Research Letters, 42(11), 4335-4342.
- Mao, Z., Wang, F., Lin, J.-F., Fu, S., Yang, J., Wu, X., Okuchi, T., Tomioka, N., Prakapenka, V.B., and Xiao,
 Y. (2017) Equation of state and hyperfine parameters of high-spin bridgmanite in the Earth's
 lower mantle by synchrotron X-ray diffraction and Mössbauer spectroscopy. American
 Mineralogist, 102(2), 357-368.
- 498 Masters, G., Laske, G., Bolton, H., and Dziewonski, A. (2000) The relative behavior of shear velocity, 499 bulk sound speed, and compressional velocity in the mantle: implications for chemical and

- thermal structure. Earth's deep interior: mineral physics and tomography from the atomic to the global scale, 63-87.
- McCammon, C., Dubrovinsky, L., Narygina, O., Kantor, I., Wu, X., Glazyrin, K., Sergueev, I., and Chumakov, A. (2010) Low-spin Fe²⁺ in silicate perovskite and a possible layer at the base of the lower mantle. Physics of the Earth and Planetary Interiors, 180(3), 215-221.

506

507 508

509

510

511

512513

514515

516

517

518

519

520

521

522

523

524

525

526

527

528

529

530

531

532

533534

535

- Momma, K., and Izumi, F. (2011) VESTA 3 for three-dimensional visualization of crystal, volumetric and morphology data. Journal of applied crystallography, 44(6), 1272-1276.
- Murakami, M., Ohishi, Y., Hirao, N., and Hirose, K. (2012) A perovskitic lower mantle inferred from high-pressure, high-temperature sound velocity data. Nature, 485(7396), 90-4.
- Narygina, O.V., Kantor, I.Y., McCammon, C., and Dubrovinsky, L. (2010) Electronic state of Fe²⁺ in (Mg, Fe)(Si, Al) O3 perovskite and (Mg,Fe)SiO₃ majorite at pressures up to 81 GPa and temperatures up to 800 K. Physics and Chemistry of Minerals, 37(6), 407-415.
- O'keeffe, M., Hyde, B.J.A.C.S.B.S.C., and Chemistry, C. (1977) Some structures topologically related to cubic perovskite (E21), ReO3 (D09) and Cu3Au (L12). 33(12), 3802-3813.
- Petříček, V., Dušek, M., and Palatinus, L. (2014) Crystallographic computing system JANA2006: general features. Zeitschrift für Kristallographie-Crystalline Materials, 229(5), 345-352.
- Poitrasson, F., Halliday, A.N., Lee, D.-C., Levasseur, S., and Teutsch, N. (2004) Iron isotope differences between Earth, Moon, Mars and Vesta as possible records of contrasted accretion mechanisms. Earth and Planetary Science Letters, 223(3-4), 253-266.
- Ringwood, A.E. (1975) Composition and petrology of the earth's mantle [by] AE Ringwood.
- Ross, N.L., Hazen, R.M.J.P., and Minerals, C.o. (1990) High-pressure crystal chemistry of MgSiO 3 perovskite. 17(3), 228-237.
- Sasaki, S., Prewitt, C.T., and Liebermann, R.C. (1983) The crystal structure of CaGeO₃ perovskite and the crystal chemistry of the GdFeO₃-type perovskites. American Mineralogist, 68(11-12), 1189-1198.
- Schelling, P.K., Phillpot, S.R., and Keblinski, P. (2002) Comparison of atomic-level simulation methods for computing thermal conductivity. Physical Review B, 65(14), 144306.
 - Shukla, G., Cococcioni, M., and Wentzcovitch, R.M. (2016) Thermoelasticity of Fe³⁺-and Al-bearing bridgmanite: Effects of iron spin crossover. Geophysical Research Letters, 43(11), 5661-5670.
- Shukla, G., and Wentzcovitch, R.M. (2016) Spin crossover in (Mg,Fe $^{3+}$)(Si,Fe $^{3+}$)O₃ bridgmanite: Effects of disorder, iron concentration, and temperature. Physics of the Earth and Planetary Interiors, 260, 53-61.
- Shukla, G., Wu, Z., Hsu, H., Floris, A., Cococcioni, M., and Wentzcovitch, R.M. (2015) Thermoelasticity of Fe²⁺-bearing bridgmanite. Geophysical Research Letters, 42(6), 1741-1749.
- Sugahara, M., Yoshiasa, A., Komatsu, Y., Yamanaka, T., Bolfan-Casanova, N., Nakatsuka, A., Sasaki, S., and Tanaka, M.J.A.M. (2006) Reinvestigation of the MgSiO₃ perovskite structure at high pressure. 91(4), 533-536.
- Toby, B.H. (2006) R factors in Rietveld analysis: How good is good enough? Powder Diffraction, 21(1), 67-70.
- Tsuchiya, T., and Wang, X. (2013) Ab initio investigation on the high-temperature thermodynamic properties of Fe³⁺-bearing MgSiO³ perovskite. Journal of Geophysical Research: Solid Earth, 118(1), 83-91.
- Vanpeteghem, C., Zhao, J., Angel, R., Ross, N., and Bolfan-Casanova, N. (2006) Crystal structure and equation of state of MgSiO3 perovskite. Geophysical Research Letters, 33(3).
- Yang, H., Lin, J.-F., Hu, M.Y., Roskosz, M., Bi, W., Zhao, J., Alp, E.E., Liu, J., Liu, J., and Wentzowitch, R.M.
 (2019) Iron isotopic fractionation in mineral phases from Earth's lower mantle: Did terrestrial
 magma ocean crystallization fractionate iron isotopes? Earth and Planetary Science Letters,
 506, 113-122.
- Zhao, Y., Weidner, D.J., Parise, J.B., Cox, D.E.J.P.o.t.E., and Interiors, P. (1993a) Thermal expansion and
 structural distortion of perovskite—data for NaMgF3 perovskite. Part I. 76(1-2), 1-16.

Figures and Tables:

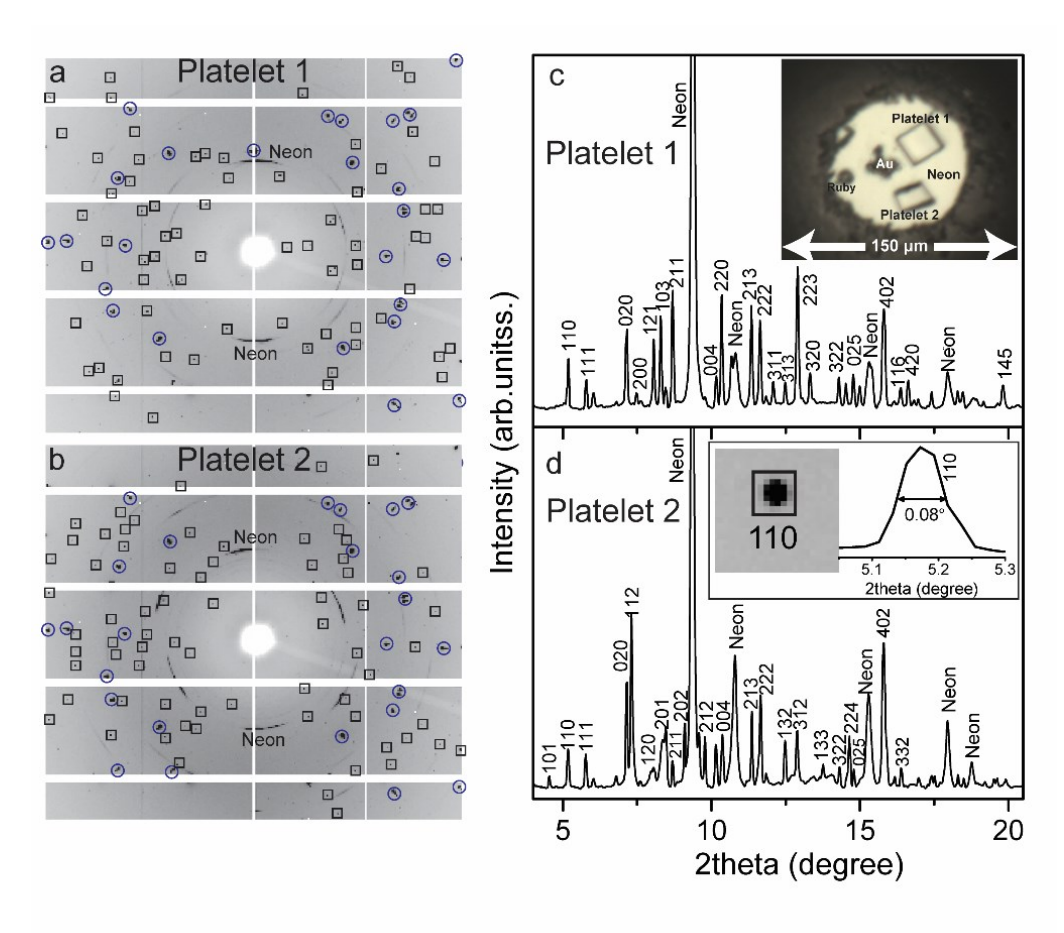


Figure 1. Representative single-crystal X-ray diffraction results of Fe10-Al14-Bgm at ~52.7 GPa and room temperature. **a** and **b** Original XRD patterns of platelets 1 and 2, respectively. The black squares and blue circles mark reflection spots from bridgmanite and diamonds, respectively. Diffraction rings show signals from solid neon medium, labeled with "Neon". **c** and **d** Corresponding integrated XRD patterns of platelets 1 and 2, respectively. Miller indices (hkl) of bridgmanite are labeled close to the top of diffraction peaks. The average FWHM of these peaks is ~0.08°. The insert in **c** shows an image of the sample chamber with two Fe10-Al14-Bgm platelets and Au pressure calibrant. The insert in **d** is a round 110 reflection spot and its integrated peak. The wavelength of the incident X-ray beam is 0.2952 Å.

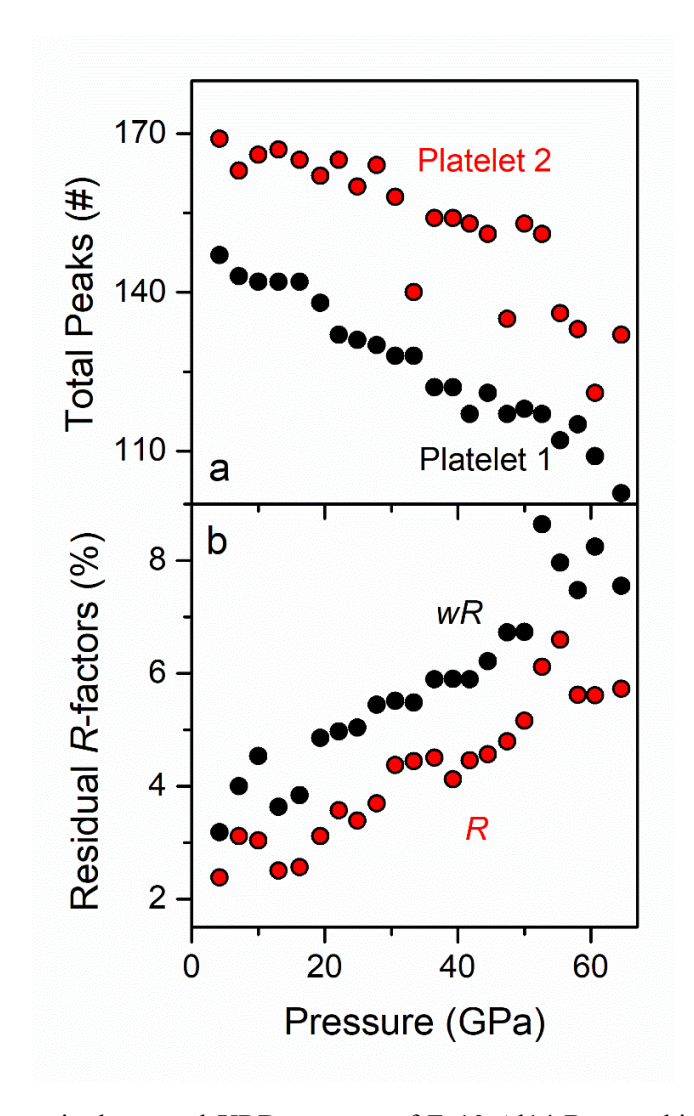


Figure 2. Data analyses on single-crystal XRD patterns of Fe10-Al14-Bgm at high pressure. **a** The number of high-quality reflection peaks of each bridgmanite platelet used for structure refinements. These reflections were selected with intensities (*I*) of $I > 3\sigma(I)$. Solid black and red circles are for platelets 1 and 2, respectively. **b** Residual *R*-factors during the refinements to derive the atomic structure of Fe10-Al14-Bgm using JANA software (Petříček et al., 2014). Solid black and red circles show weighted *R*-factor ($wR(F^2)$) and *R*-factor ($wR(F^2)$) in percentages, respectively.

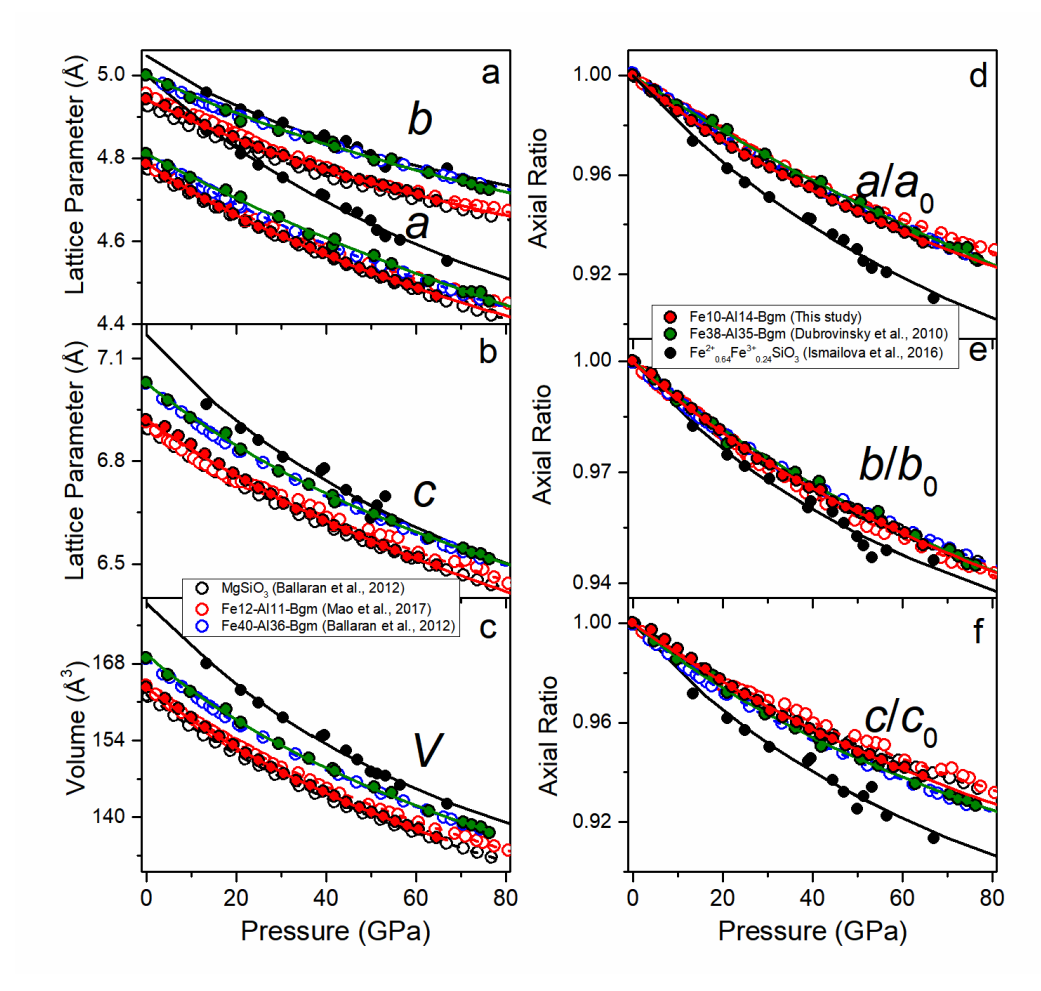


Figure 3. Unit-cell parameters of single-crystal Fe10-Al14-Bgm at high pressure. **a-c** Lattice parameters (a, b, c) and unit-cell volume (V). **d-f** Normalized lattice parameters $(a/a_0, b/b_0, \text{ and } c/c_0, \text{ respectively})$. Solid red circles are results of Fe10-Al14-Bgm in this study, and representative previous data on bridgmanite with different Fe and Al contents are plotted for comparisons (Boffa Ballaran et al., 2012; Dubrovinsky et al., 2010; Ismailova et al., 2016; Mao et al., 2017). Particularly, solid symbols are single-crystal XRD data on bridgmanite with well-resolved atomic coordinates (Dubrovinsky et al., 2010; Ismailova et al., 2016), while open symbols are on samples derived from integrated XRD patterns (Boffa Ballaran et al., 2012; Mao et al., 2017).

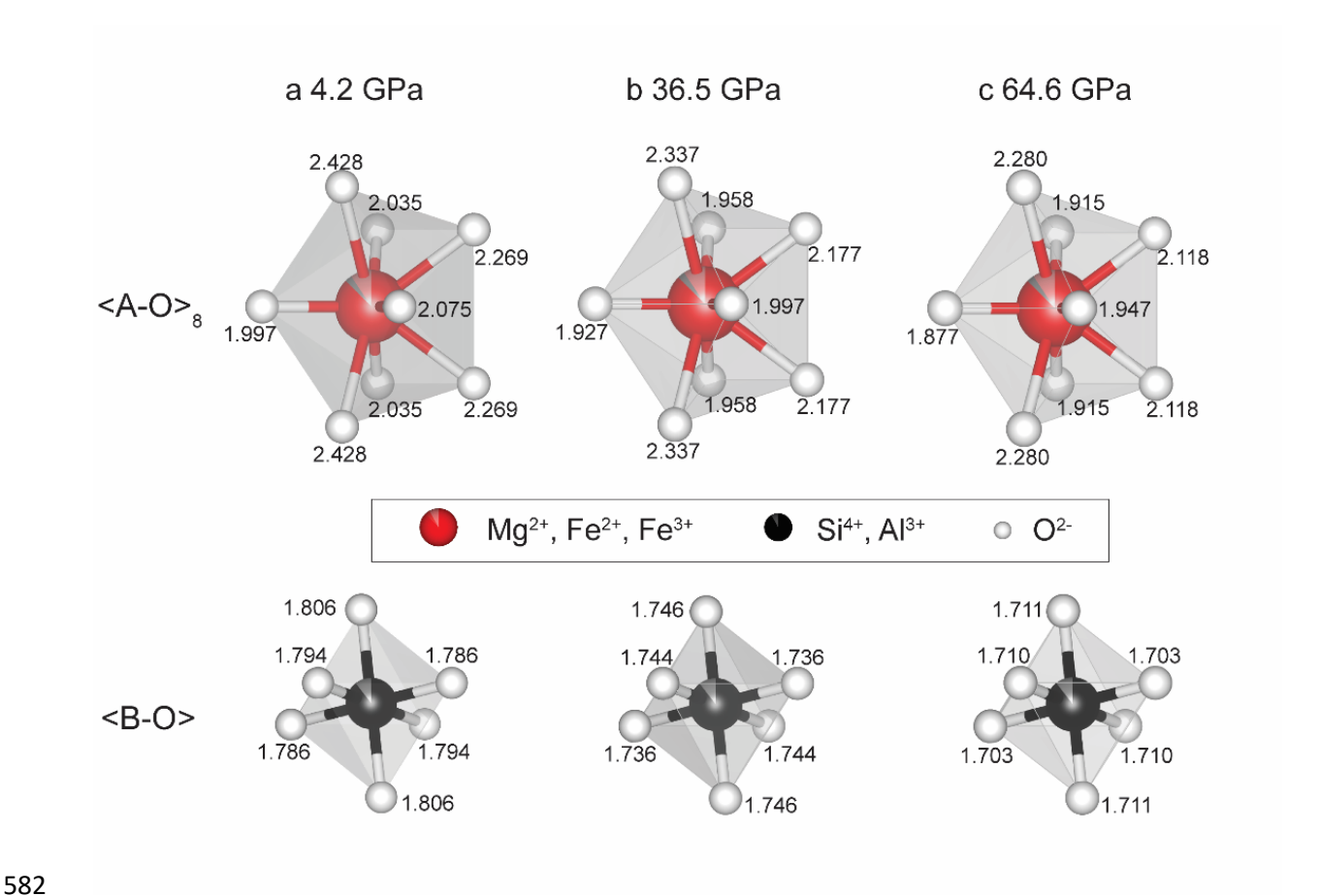


Figure 4. Local atomic configurations and bond lengths around the A-site and B-site atoms in single-crystal Fe10-Al14-Bgm at high pressure. **a** 4.2 GPa. **b** 36.5 GPa. **c** 64.6 GPa. Red, black, and white balls represent A-site, B-site, and oxygen atoms, respectively. These structures are viewed and graphed from *a* axis. The upper and lower panels show configurations of A-site and B-site atoms, respectively. Numbers next to the oxygen atoms are respective bond lengths with a unit of Å.

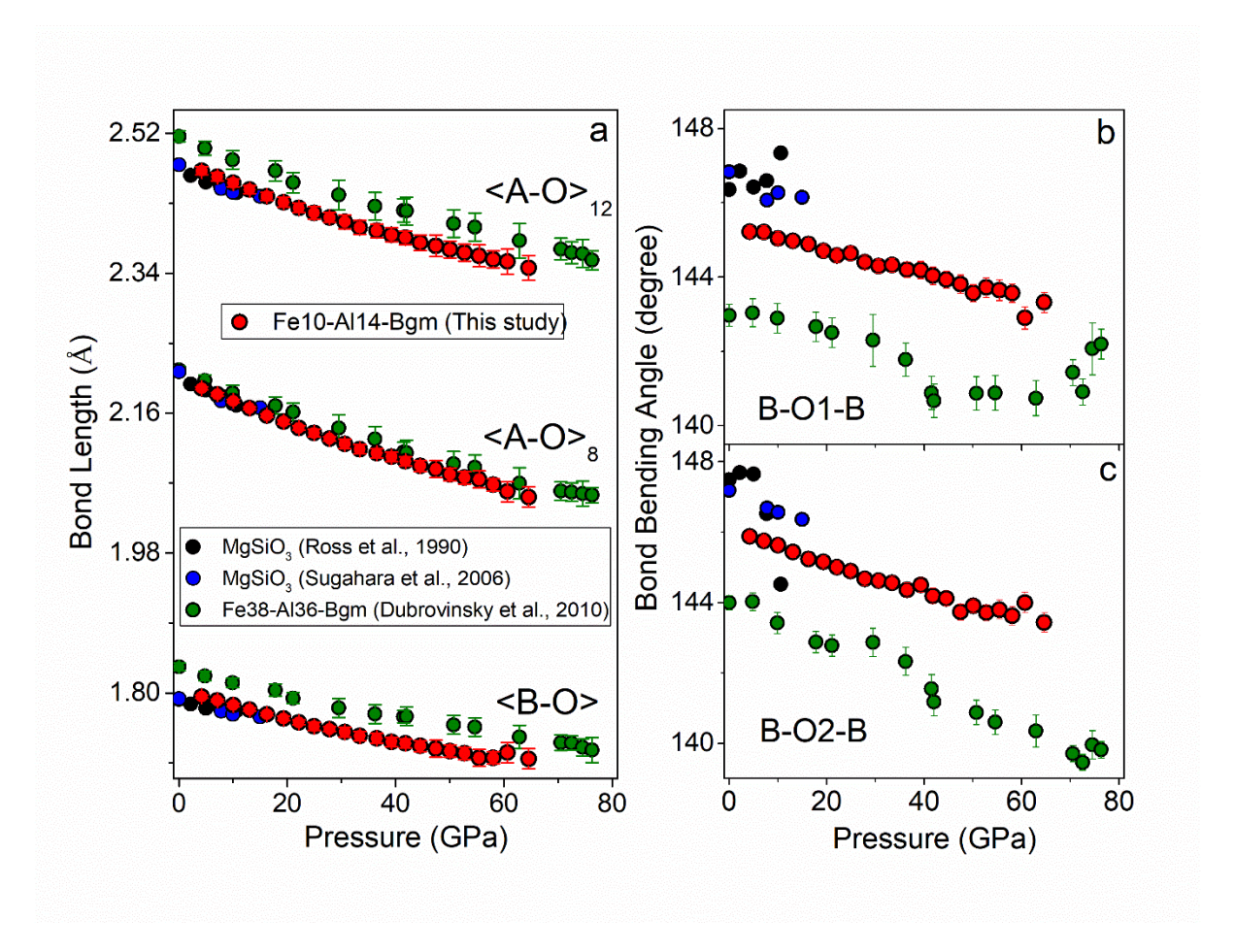


Figure 5. Interatomic distances and angles in the structure of single-crystal Fe10-Al14-Bgm as a function of pressure. **a** Atomic distances of the A-site and B-site atoms with respect to oxygen atoms. <A-O>₁₂ and <A-O>₈ are average distances between O and A-site atoms in eightfold and twelvefold coordination, respectively, while <B-O> are average distances between O and B-site atoms in sixfold coordination. **b** and **c** Variations of BO₆ octahedral tilt angles in the *b-c* plane and the *a-b* plane, given by B-O1-B and B-O2-B, respectively. Solid red circles are results of single-crystal Fe10-Al14-Bgm in this study, and previous data on bridgmanite with different compositions are plotted for comparisons (Dubrovinsky et al., 2010; Ross et al., 1990; Sugahara et al., 2006). The decrease of B-O1-B and B-O2-B angles with pressure indicates an increased distortion of the orthorhombic structure.

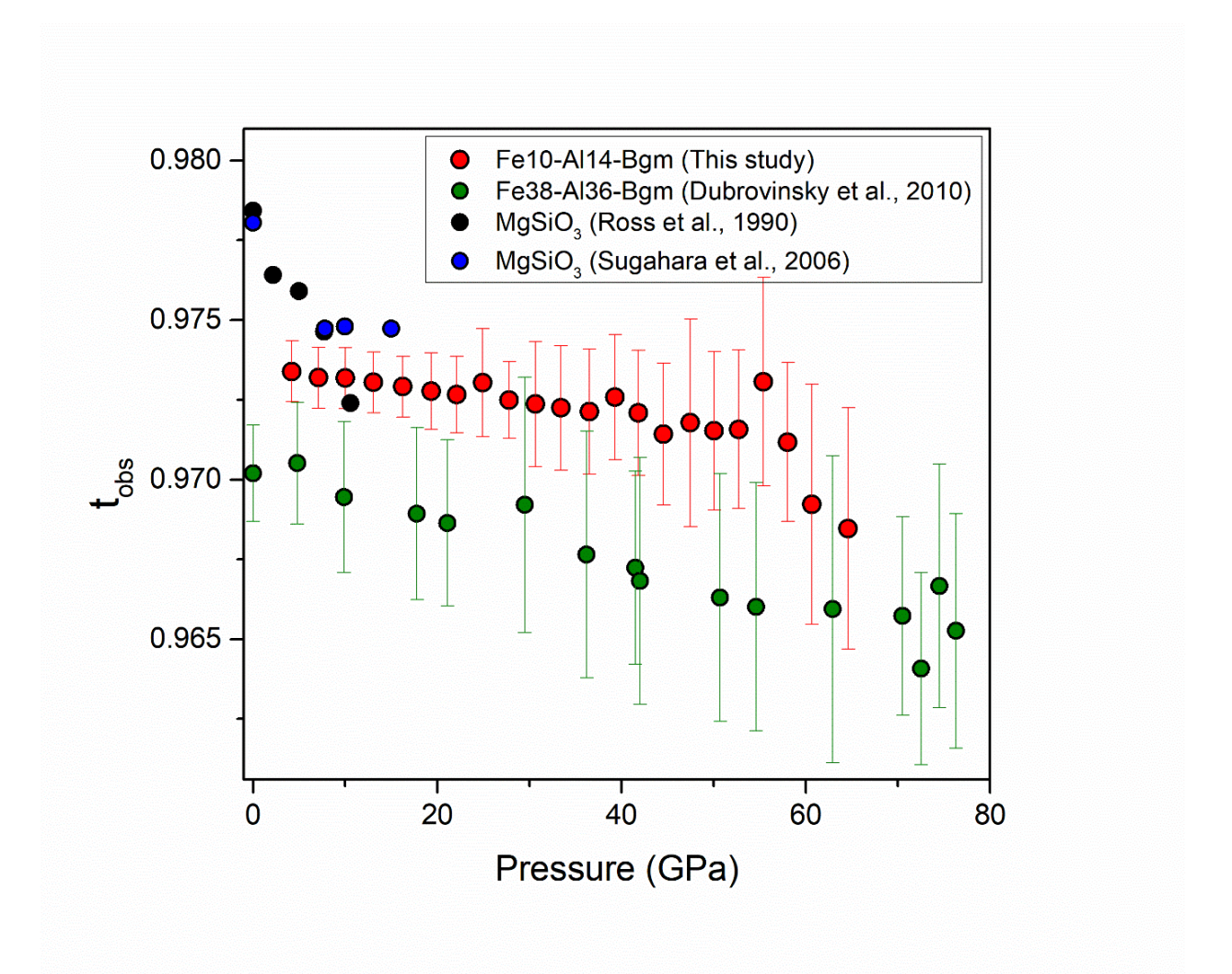


Figure 6. The tolerance factors (t_{obs}) of single-crystal Fe10-Al14-Bgm as function of pressure. Solid red circles are results from this study, and literature data on bridgmanite with different compositions are plotted for comparisons (Dubrovinsky et al., 2010; Ross et al., 1990; Sugahara et al., 2006). Deviations of t_{obs} from one indicate a distortion of the bridgmanite structure from an ideal GdFeO₃-type cubic symmetry (Sasaki et al., 1983).

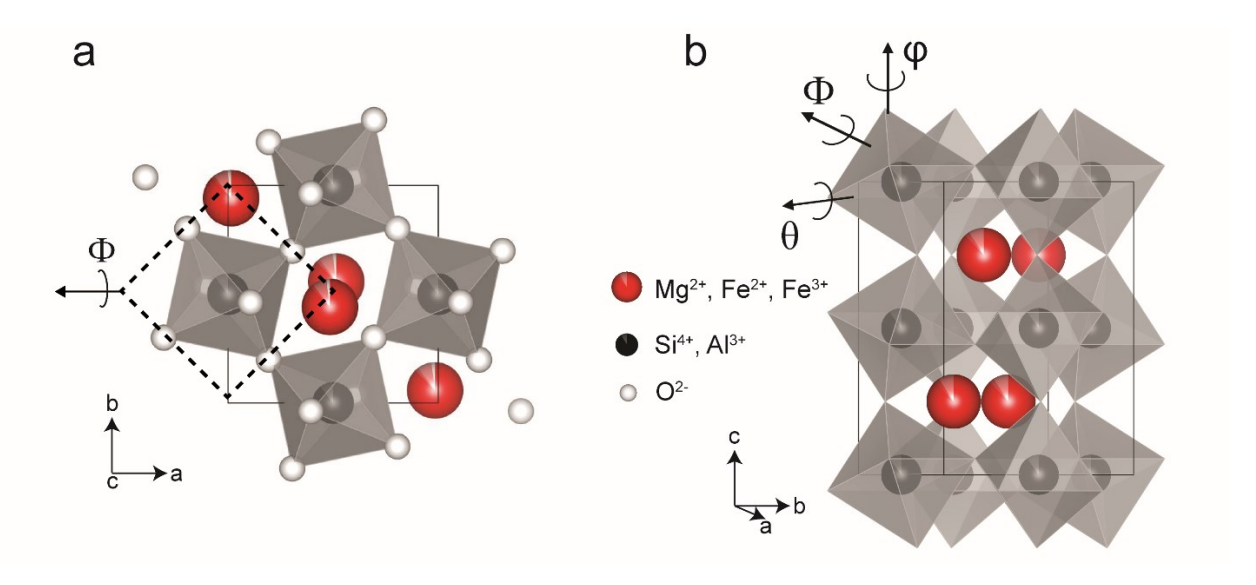


Figure 7. Schematic illustrations of the octahedral titling angles (Φ) in the structure of single-crystal Fe10-Al14-Bgm at 64.6 GPa. **a** Top view from c axis; **b** Side view. The octahedron in bridgmanite structure can be assumed as a pseudo-cubic unit cell, shown as dashed square in **a**. Φ is defined as titling of the octahedron about the pseudo-cubic [111] direction. Φ can be also viewed as a combination of titling about the pseudo-cubic [110] direction (angle θ) and the pseudo-cubic [001] direction (angle φ), shown in **b**. Refer to Figure 4 for detailed geometry of the octahedron in single-crystal Fe10-Al14-Bgm viewing from a axis at different high pressures.

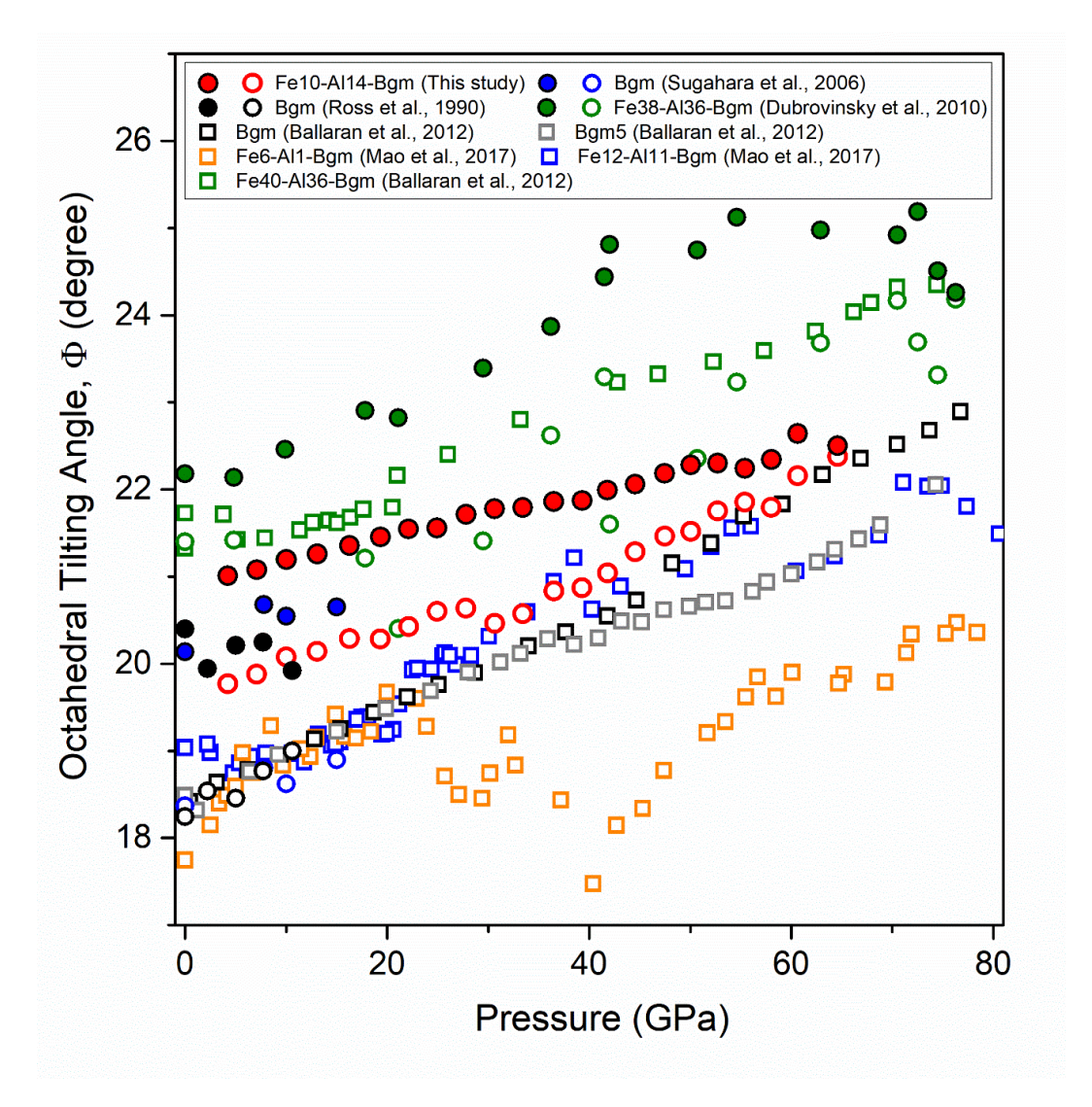


Figure 8. Octahedral titling angles in the single-crystal Fe10-Al14-Bgm as a function of pressure. Red circles are results of Fe10-Al14-Bgm in this study, and literature reports on bridgmanite with different compositions are plotted for comparisons (Boffa Ballaran et al., 2012; Dubrovinsky et al., 2010; Mao et al., 2017; Ross et al., 1990; Sugahara et al., 2006). Solid symbols are derived from the quantitatively refined atomic coordinates in a microscopic approach, while open symbols are calculations from lattice parameters in a macroscopic approach. Bgm denotes MgSiO₃ bridgmanite end member.

Table 1. Refined unit-cell parameters and atomic coordinates of single-crystal Fe10-Al14-Bgm at high pressures

Pressure (GPa)	Evaluation parameters		Unit-cell parameters			A site				B site				01				O2			
	*Total peaks (#)	wR (%)	a (Å)	b (Å)	c (Å)	X	у	Z	U	X	у	z	U	X	у	Z	U	X	у	Z	U
4.2(1)	316	3.2	4.7564(7)	4.9263(4)	6.9005(9)	0.5149(1)	0.5583(1)	0.25	0.0066(2)	0.5	0	0.5	0.0041(2)	0.1068(2)	0.4631(2)	0.25	0.0056(4)	0.1943(2)	0.1994(1)	0.5548(2)	0.0060(3)
7.1(2)	306	4.0	4.7378(10)	4.9098(4)	6.8742(9)	0.5151(1)	0.5588(2)	0.25	0.0056(3)	0.5	0	0.5	0.0031(2)	0.1070(3)	0.4633(2)	0.25	0.0048(5)	0.1939(2)	0.1992(2)	0.5548(2)	0.0051(4)
10.0(2)	308	4.5	4.7191(7)	4.8949(4)	6.8493(9)	0.5154(1)	0.5594(2)	0.25	0.0053(3)	0.5	0	0.5	0.0029(2)	0.1076(3)	0.4629(2)	0.25	0.0042(5)	0.1935(2)	0.1985(2)	0.5550(2)	0.0049(4)
13.1(2)	309	3.6	4.7006(6)	4.8792(4)	6.8205(15)	0.5157(1)	0.5601(2)	0.25	0.0052(2)	0.5	0	0.5	0.0030(2)	0.1079(2)	0.4631(2)	0.25	0.0043(4)	0.1931(2)	0.1983(1)	0.5554(2)	0.0047(3)
16.3(2)	307	3.8	4.6816(7)	4.8648(4)	6.7918(12)	0.5159(1)	0.5609(2)	0.25	0.0063(2)	0.5	0	0.5	0.0043(2)	0.1082(2)	0.4632(2)	0.25	0.0055(4)	0.1926(2)	0.1978(1)	0.5556(2)	0.0060(3)
19.3(2)	300	4.8	4.6657(9)	4.8511(5)	6.7648(11)	0.5162(1)	0.5614(2)	0.25	0.0049(3)	0.5	0	0.5	0.0031(2)	0.1088(3)	0.4633(2)	0.25	0.0045(5)	0.1922(2)	0.1978(2)	0.5557(2)	0.0042(4)
22.1(3)	297	5.0	4.6492(14)	4.8362(6)	6.7435(11)	0.5164(1)	0.5620(2)	0.25	0.0047(3)	0.5	0	0.5	0.0031(2)	0.1093(3)	0.4635(2)	0.25	0.0042(5)	0.1917(2)	0.1975(2)	0.5558(2)	0.0044(4)
24.9(3)	291	5.0	4.6342(8)	4.8257(4)	6.7225(11)	0.5166(1)	0.5627(2)	0.25	0.0044(3)	0.5	0	0.5	0.0027(2)	0.1091(3)	0.4635(2)	0.25	0.0036(6)	0.1916(2)	0.1972(2)	0.5560(2)	0.0036(4)
27.8(3)	294	5.4	4.6208(11)	4.8127(12)	6.7035(11)	0.5169(1)	0.5635(2)	0.25	0.0046(3)	0.5	0	0.5	0.0029(2)	0.1100(3)	0.4633(2)	0.25	0.0038(6)	0.1909(2)	0.1968(2)	0.5563(2)	0.0040(4)
30.6(3)	286	5.5	4.6107(20)	4.8054(7)	6.6765(15)	0.5172(2)	0.5639(2)	0.25	0.0036(3)	0.5	0	0.5	0.0024(2)	0.1101(3)	0.4633(3)	0.25	0.0041(6)	0.1908(2)	0.1965(2)	0.5562(2)	0.0031(4)
33.4(7)	268	5.5	4.5955(14)	4.7896(6)	6.6595(14)	0.5174(2)	0.5645(2)	0.25	0.0032(4)	0.5	0	0.5	0.0016(2)	0.1103(3)	0.4635(3)	0.25	0.0038(6)	0.1905(2)	0.1966(2)	0.5563(2)	0.0033(5)
36.5(4)	276	5.9	4.5835(17)	4.7832(10)	6.6450(18)	0.5177(2)	0.5647(2)	0.25	0.0040(4)	0.5	0	0.5	0.0029(2)	0.1110(4)	0.4637(3)	0.25	0.0044(7)	0.1900(3)	0.1963(2)	0.5566(3)	0.0038(5)
39.3(4)	276	5.9	4.5725(15)	4.7743(8)	6.627(12)	0.5178(2)	0.5655(3)	0.25	0.0053(4)	0.5	0	0.5	0.0033(2)	0.1111(4)	0.4639(3)	0.25	0.0050(8)	0.1902(3)	0.1963(2)	0.5565(3)	0.0048(6)
41.8(4)	270	5.9	4.5618(23)	4.7698(9)	6.6100(20)	0.5182(2)	0.5660(3)	0.25	0.0058(5)	0.5	0	0.5	0.0042(2)	0.1113(4)	0.4637(3)	0.25	0.0057(8)	0.1897(3)	0.1959(3)	0.5570(3)	0.0055(6)
45.6(5)	272	6.2	4.5470(14)	4.7546(8)	6.5990(22)	0.5184(2)	0.5661(3)	0.25	0.0061(5)	0.5	0	0.5	0.0046(2)	0.1122(5)	0.4641(3)	0.25	0.0063(7)	0.1893(3)	0.1957(3)	0.5569(3)	0.0062(6)
47.5(5)	242	6.7	4.5353(12)	4.7480(7)	6.5820(15)	0.5186(2)	0.5668(3)	0.25	0.0070(5)	0.5	0	0.5	0.0058(2)	0.1125(5)	0.4635(4)	0.25	0.0067(8)	0.1883(4)	0.1953(2)	0.5577(4)	0.0066(7)
50.1(4)	271	6.7	4.5254(14)	4.7436(9)	6.5620(23)	0.5188(2)	0.5677(3)	0.25	0.0068(4)	0.5	0	0.5	0.0059(2)	0.1133(4)	0.4638(3)	0.25	0.0064(7)	0.1883(3)	0.1953(2)	0.5572(3)	0.0065(5)
52.7(4)	268	8.6	4.5142(12)	4.7342(7)	6.5530(14)	0.5190(2)	0.5677(3)	0.25	0.0067(5)	0.5	0	0.5	0.0063(2)	0.1130(6)	0.4641(4)	0.25	0.0055(9)	0.1874(4)	0.1951(3)	0.5574(4)	0.0054(7)
55.4(5)	235	8.0	4.5044(17)	4.7268(8)	6.5395(13)	0.5193(3)	0.5684(4)	0.25	0.0103(6)	0.5	0	0.5	0.0096(2)	0.1128(6)	0.4632(5)	0.25	0.0100(9)	0.1891(4)	0.1951(3)	0.5577(5)	0.0097(8)
58.0(5)	240	7.5	4.4962(12)	4.7206(7)	6.5215(18)	0.5194(3)	0.5687(3)	0.25	0.0063(5)	0.5	0	0.5	0.0055(2)	0.1136(5)	0.4642(4)	0.25	0.0058(8)	0.1878(4)	0.1949(3)	0.5579(5)	0.0059(7)
60.6(6)	193	8.2	4.4858(12)	4.7127(8)	6.5190(19)	0.5195(3)	0.5691(4)	0.25	0.0046(8)	0.5	0	0.5	0.0045(2)	0.1156(8)	0.4642(6)	0.25	0.0053(12)	0.1876(5)	0.1948(4)	0.5576(6)	0.0052(5)
64.6(6)	234	7.6	4.4669(15)	4.6972(9)	6.4955(24)	0.5199(3)	0.5701()	0.25	0.0059(6)	0.5	0	0.5	0.0039(2)	0.1148(6)	0.4643(5)	0.25	0.0066(10)	0.1878(4)	0.1944(4)	0.5580(5)	0.0066(8)

^{*:} The total number of used peaks on two crystal platelets together. The reflections have intensities (I) of $I > 3\sigma(I)$ for structure refinements. Refer to Figure 2a for the number of used peaks on individual platelet.

Table 2. Selected interatomic distances (Å) and angles (°) in the structure of single-crystal Fe10-Al14-Bgm at high pressures

Pressure (GPa)	B-O1 × 2 (Å)	B-O2 × 2 (Å)	B-O2 × 2 (Å)	Mean <b-o> (Å)</b-o>	A-O1 × 1 (Å)	A-O1 × 1 (Å)	A-O1 × 1 (Å)	A-O1 × 1 (Å)	A-O2 × 2 (Å)	A-O2 × 2 (Å)	A-O2 × 2 (Å)	A-O2 × 2 (Å)	Mean <a-o>viii (Å)</a-o>	Mean <a-o>xii (Å)</a-o>	B-O1-B (°)	B-O2-B (°)
4.2(1)	1.806(1)	1.794(1)	1.786(1)	1.795(1)	1.997(1)	2.854(2)	2.988(1)	2.075(1)	3.141(2)	2.269(1)	2.428(2)	2.035(1)	2.192(1)	2.471(1)	145.2(2)	145.9(2)
7.1(2)	1.801(1)	1.789(1)	1.781(1)	1.790(1)	1.990(2)	2.843(2)	2.981(1)	2.068(1)	3.135(2)	2.262(1)	2.419(2)	2.028(1)	2.184(1)	2.464(1)	145.2(2)	145.7(2)
10.0(2)	1.795(1)	1.783(1)	1.776(1)	1.785(1)	1.981(2)	2.834(2)	2.977(1)	2.059(1)	3.129(2)	2.253(1)	2.408(2)	2.021(2)	2.176(1)	2.456(1)	145.0(2)	145.6(2)
13.1(2)	1.788(1)	1.778(1)	1.770(1)	1.779(1)	1.975(1)	2.824(1)	2.970(1)	2.050(1)	3.123(1)	2.242(1)	2.399(1)	2.012(1)	2.166(1)	2.447(1)	145.0(2)	145.4(2)
16.3(2)	1.781(1)	1.773(1)	1.765(1)	1.773(1)	1.967(1)	2.813(1)	2.965(1)	2.042(1)	3.117(1)	2.232(1)	2.389(2)	2.003(1)	2.157(1)	2.439(1)	144.9(2)	145.2(2)
19.3(2)	1.775(2)	1.768(1)	1.760(1)	1.767(2)	1.960(2)	2.806(2)	2.959(1)	2.035(1)	3.110(2)	2.223(2)	2.379(2)	1.996(2)	2.149(2)	2.431(2)	144.7(2)	145.1(2)
22.1(3)	1.770(1)	1.763(1)	1.754(1)	1.762(1)	1.951(2)	2.798(2)	2.953(2)	2.028(1)	3.105(2)	2.215(1)	2.371(2)	1.988(1)	2.141(2)	2.424(2)	144.6(2)	145.0(2)
24.9(3)	1.764(2)	1.758(1)	1.751(1)	1.757(2)	1.948(2)	2.787(2)	2.950(2)	2.020(2)	3.100(2)	2.207(2)	2.363(2)	1.983(2)	2.134(3)	2.418(3)	144.6(2)	144.9(2)
27.8(3)	1.760(1)	1.755(1)	1.746(1)	1.754(1)	1.941(2)	2.783(2)	2.947(2)	2.012(2)	3.098(2)	2.200(2)	2.356(2)	1.976(2)	2.127(3)	2.410(3)	144.4(2)	144.7(2)
30.6(3)	1.753(2)	1.751(1)	1.744(1)	1.750(2)	1.938(2)	2.776(2)	2.944(2)	2.008(2)	3.092(2)	2.193(2)	2.348(3)	1.969(2)	2.120(3)	2.406(2)	144.3(2)	144.6(2)
33.4(7)	1.749(1)	1.747(1)	1.737(1)	1.745(1)	1.932(2)	2.767(2)	2.938(2)	1.999(2)	3.086(2)	2.185(2)	2.340(2)	1.965(2)	2.113(3)	2.399(3)	144.3(2)	144.6(2)
36.5(4)	1.746(2)	1.744(2)	1.735(1)	1.742(2)	1.926(2)	2.761(2)	2.935(2)	1.997(2)	3.085(2)	2.177(2)	2.337(3)	1.958(2)	2.109(4)	2.394(4)	144.2(2)	144.4(2)
39.3(4)	1.741(2)	1.739(2)	1.732(1)	1.737(2)	1.923(2)	2.755(3)	2.932(2)	1.991(2)	3.078(3)	2.172(2)	2.328(3)	1.958(2)	2.104(3)	2.389(3)	144.2(2)	144.5(2)
41.8(4)	1.737(2)	1.738(2)	1.730(2)	1.735(2)	1.919(3)	2.750(3)	2.933(3)	1.987(2)	3.079(3)	2.166(2)	2.323(3)	1.950(2)	2.098(4)	2.385(4)	144.0(2)	144.2(2)
45.6(5)	1.735(2)	1.733(2)	1.725(2)	1.732(2)	1.910(2)	2.743(2)	2.923(2)	1.983(2)	3.073(3)	2.161(2)	2.318(3)	1.944(2)	2.092(4)	2.379(4)	143.9(2)	144.1(2)
47.5(5)	1.731(2)	1.733(2)	1.722(2)	1.728(2)	1.907(3)	2.737(3)	2.925(2)	1.976(2)	3.075(3)	2.154(2)	2.314(4)	1.936(2)	2.088(4)	2.375(4)	143.8(2)	143.7(2)
50.1(4)	1.727(3)	1.728(2)	1.719(2)	1.725(2)	1.900(2)	2.735(3)	2.925(2)	1.972(2)	3.068(3)	2.149(2)	2.304(4)	1.936(2)	2.081(4)	2.370(4)	143.6(2)	143.9(3)
52.7(4)	1.724(3)	1.727(2)	1.715(2)	1.722()	1.899(3)	2.725(3)	2.920(3)	1.968(3)	3.066(3)	2.148(3)	2.299(4)	1.930(3)	2.077(3)	2.366(3)	143.7(3)	143.7(3)
55.4(5)	1.721(3)	1.719(3)	1.716(2)	1.717(3)	1.898(3)	2.719(3)	2.922(3)	1.959(3)	3.062(4)	2.136(3)	2.298(5)	1.929(3)	2.075(4)	2.362(3)	143.6(3)	143.8(3)
58.0(5)	1.716(3)	1.719(3)	1.712(2)	1.717(3)	1.891(3)	2.715(3)	2.915(2)	1.960(2)	3.059(4)	2.133(3)	2.292(4)	1.922(3)	2.068(4)	2.358(4)	143.6(3)	143.6(3)
60.6(6)	1.719(3)	1.716(2)	1.705(2)	1.723(3)	1.875(4)	2.722(4)	2.915(3)	1.958(3)	3.052(4)	2.135(3)	2.279(5)	1.928(4)	2.059(5)	2.355(5)	142.9(3)	144.0(3)
64.6(6)	1.711(3)	1.710(2)	1.703(2)	1.715(3)	1.878(3)	2.702(3)	2.908(3)	1.947(3)	3.052(4)	2.118(3)	2.279(5)	1.915(3)	2.052(5)	2.347(5)	143.3(3)	143.4(3)